EDGE ARTICLE

Check for updates

Theoretical insights into the generation and reactivity of hydride on the ZnO(10$\bar{1}$0) surface†

Xian-Yang Zhang,[a] Zhi-Qiang Wang[*a] and Xue-Qing Gong [ID] [*b]

ZnO is an important catalytic material for CO/CO$_2$ hydrogenation. In this work, the pristine ZnO(10$\bar{1}$0) and the surfaces with Zn–O dimer vacancies (ZnO(10$\bar{1}$0)–(Zn–O)$_{DiV}$) and oxygen vacancies are calculated. We find that the hydride (H$^-$) species can be generated *via* heterolytic H$_2$ dissociation on these surfaces, and that ZnO(10$\bar{1}$0)–(Zn–O)$_{DiV}$ only needs to overcome the energy barrier of ~0.10 eV. This is because the ZnO system has flexible orbitals for electron storage and release and the low-coordinated Zn$_{3c}$ atoms at the defect sites can form stable Zn–H$^-$ covalent bonds with high symmetry. Flexible Zn orbitals also impart the unique feature of activating multiple electrophilic adsorbates simultaneously as excess electrons exist. Moreover, we show that the covalent Zn–H$^-$ species can regulate the catalytic activity and selectivity for CO$_2$ hydrogenation by preferentially producing *HCOO intermediates at Zn–O dimer vacancies. These results may help in the design of efficient Zn-based hydrogenation catalysts.

Introduction

As a commonly used catalytic material, ZnO often plays crucial roles in catalyzing hydrogenation reactions, such as CO$_2$ selective hydrogenation to methanol and conversion of syngas (mixture gas of CO/CO$_2$/H$_2$) to light olefins.[1–4] A deep understanding of its catalytic activities would help construct Zn-based catalysts with better performances for these reactions, which may also contribute to the control of fossil fuel usage and the realization of carbon neutrality. However, a lot of debate still remains regarding the nature of the active site for the selective hydrogenation reactions.[5–8] For example, for the CO$_2$ selective hydrogenation catalyzed by the Cu/ZnO/Al$_2$O$_3$ catalyst, Behrens *et al.*[9] suggested that the Cu–Zn alloys could form and promote the synthetic activity toward methanol, while the metal–oxide interface formed by Cu and ZnO was proposed as the active site by Kattel *et al.*[10] Chen *et al.*[11] found that the Cu/ZnO/ZrO$_2$ catalyst can also be used for CO$_2$ selective hydrogenation reactions, and they pointed out that the ZnO–ZrO$_2$ interface is the active site, while the copper species plays the role of activating H$_2$ and providing hydrogen for the reaction. In addition, Li and co-workers[12] found that the single Cu atoms loaded on the ZnO surface can catalyze the selective hydrogenation of CO$_2$ to

methanol with the selectivity of ~99.4%, and they also suggested that the water vapor in the system can act as a bridge between surface H and CO$_2$ intermediates and has the regulatory role of increasing methanol selectivity. In general, catalysts containing ZnO have been extensively used in the selective hydrogenation reactions of CO$_2$,[8–13] and exploring its reaction mechanism is essential for further understanding their key features, especially the actual active site.

In fact, there have already been many studies about selective hydrogenation reactions on clean ZnO surfaces, which were mainly focused on the activation mechanisms of H$_2$ and CO$_2$.[13–15] Wöll and co-workers[16] studied the CO$_2$ adsorption and activation on the ZnO(10$\bar{1}$0) surface with infrared reflection absorption spectroscopy (IRRAS) and showed that CO$_2$ can be adsorbed along the [0001] direction and form the carbonate (CO$_3^{\delta-}$) species. Ling *et al.*[17] obtained the scanning tunneling microscopy (STM) images of the heterolytically dissociated H$_2$ on the ZnO(10$\bar{1}$0) surface under ambient pressure, and the adsorption structure was expected to be beneficial to the stabilization of the formed active H species. Peng and co-workers[18] examined the mechanism of H$_2$ activation on ZnO nanorods with and without surface oxygen vacancies by applying ^{17}O nuclear magnetic resonance spectroscopy (NMR), and they found that more hydride species can be produced through homolytic and heterolytic dissociation at the oxygen vacancy sites of the reduced ZnO(10$\bar{1}$0). Theoretically, Tang *et al.*[19] performed systematic on-site Coulomb interaction corrected density functional theory (DFT+U) calculations of the adsorption of CO$_2$ and found that the adsorbed CO$_2$ molecules tend to form linear structures on the polar ZnO facets (such as {0001} and {000$\bar{1}$}), while the bending structures are produced on the nonpolar ZnO facets (such as {10$\bar{1}$0}, {11$\bar{2}$0} and {11$\bar{2}$1}).

[a] State Key Laboratory of Green Chemical Engineering and Industrial Catalysis, Centre for Computational Chemistry and Research Institute of Industrial Catalysis, School of Chemistry and Molecular Engineering, East China University of Science and Technology, 130 Meilong Road, Shanghai, 200237, China. E-mail: zhiqiangwang@ecust.edu.cn

[b] School of Chemistry and Chemical Engineering, Shanghai Jiao Tong University, 800 Dongchuan Road, Shanghai, 200240, China. E-mail: xqgong@sjtu.edu.cn

† Electronic supplementary information (ESI) available. See DOI: https://doi.org/10.1039/d4sc04344h

Li and co-workers[20] calculated the pathways of H_2 activation on the pristine $ZnO(10\bar{1}0)$ surface, and they determined the heterolytic dissociation of H_2 rather than the homolytic one. Furthermore, through DFT calculations, Zhao *et al.*[21] located the complete reaction routes of CO hydrogenation to methanol on the Zn-terminated $ZnO(0001)$ surface and showed that CO would follow the route of being consecutively hydrogenated to formyl (HCO), formaldehyde (H_2CO), and methoxy (H_3CO) before the formation of methanol. Thus, we can find that the catalytic reactions at ZnO are closely related to its surface structures. However, the relationship between the unique electronic properties of ZnO and the catalytic activities in selective hydrogenation reactions has not been thoroughly investigated.

In this work, the wurtzite $ZnO(10\bar{1}0)$ surface, which has a rather low surface energy and exists under real catalytic conditions,[9] was constructed for the DFT calculations. Both the pristine and defective surfaces were considered. Specifically, the surface defect structures were confirmed by the calculated p–T phase diagrams.[6,11,22] Moreover, their electronic structures were also carefully studied, and the density of states (DOS) calculations showed a shrinkage of the unfilled dsp hybridized orbitals when excess electrons are present on the surfaces; at the same time, no new occupied states appear under the Fermi energy level (E_F), indicating a unique strategy of electron storage and release by ZnO. Systematic calculations were then performed to investigate the generation of active H species on these surfaces and their reactivities in the CO_2 selective hydrogenation reactions. It was found that the various vacancy defects are beneficial to the stabilization of the hydride species (H^-), which can be generated through the heterolytic dissociation of H_2. Interestingly, the calculated results also showed that the occurrence of H^+ (proton) from heterolytic H_2 dissociation on the $ZnO(10\bar{1}0)$ surface can be involved in activating the adsorbed H on Zn to the hydride species, and it can also help enhance the adsorption of CO_2 as well. This work revealed why the ZnO surface and its defects are favorable for catalyzing hydrogenation reactions as well as the 'multifunction role' of surface H in these reactions. It may provide some assistance for the rational design of Zn-based catalysts with high activities and selectivities.

Computational methods

In this work, all spin-polarized DFT calculations were carried out using the Vienna *Ab initio* Simulation Package (VASP).[23] The projector augmented wave (PAW)[24] method and the Perdew–Burke–Ernzerhof (PBE)[25] functional under the generalized gradient approximation (GGA)[26] were applied throughout the geometry and energy calculations. The kinetic energy cut-off was set to 400 eV, with H(1s), C(2s, 2p), O(2s, 2p) and Zn(3d, 4s) being treated as valence electrons. The force threshold in structure optimization was 0.02 eV Å^{-1}. By adopting these calculation settings, the optimized lattice constants of ZnO are $a = b = 3.26$ Å and $c = 5.24$ Å, which is in good agreement with the experimental values of $a = b = 3.25$ Å, and $c = 5.21$ Å.[27] For the model construction, we built a $p(4 \times 3)$ surface slab containing three O–Zn atomic layers for the $ZnO(10\bar{1}0)$ surface, and

the top two layers were allowed to fully relax, while the bottom O–Zn layer was kept fixed to mimic the bulk region. We used a large vacuum of ~12 Å to eliminate the interactions between neighboring slabs, and hence a k-point mesh of $2 \times 2 \times 1$ was applied to the system. Since the valence shells of Zn are filled with d and s electrons, which are strongly correlated, the properties relevant to the electronic structures were calculated by the hybrid functional raised by Heyd, Scuseria and Ernzerhof (HSE06),[30] which may give reliable electronic information and avoid errors from the unique deep-lying 3d electron distribution of Zn.[20,31]

The transition states (TSs) of surface reactions were located using a constrained optimization scheme and were verified when (i) all forces on the relaxed atoms vanish and (ii) the total energy is a maximum along the reaction coordinate, but it is a minimum with respect to the rest of the degrees of freedom.[32,33]

The adsorption energies of different species (X) on the surface ($E_{ads}(X)$) were calculated with:

$$E_{ads}(X) = -(E_{X/slab} - E_{slab} - E_X) \tag{1}$$

where $E_{X/slab}$ represents the total energy of the adsorption system, while E_{slab} and E_X are the calculated energies of the slab and the gas-phase molecular X, respectively. Note that for E_H, it was calculated with respect to half of the energy of a H_2 molecule ($1/2E_{H_2}$). Obviously, the positive adsorption energy value indicates an exothermic adsorption process, and the more positive it is, the stronger the binding between the adsorbate and the surface is.

In addition, we also calculated the formation energies of different defects of ZnO surfaces.[34] Firstly, the oxygen vacancy formation energy ($E_f^{O_v}$) was calculated as:

$$E_f^{O_v} = E_{slab}^{O_v} + \frac{1}{2}E_{mol}^{O_2} - E_{slab}^{pristine} + \Delta\mu_O \tag{2}$$

where the difference in chemical potential of an O_2 molecule under given conditions and standard conditions ($\Delta\mu_O$) was calculated as:

$$\Delta\mu_O = \mu_O - \mu_O^\theta = RT \ln \frac{P}{P^\theta} \tag{3}$$

and $E_{slab}^{O_v}$ is the total energy of the surface containing a single oxygen vacancy, $E_{mol}^{O_2}$ is the energy of a gas-phase O_2 molecule and $E_{slab}^{pristine}$ is the total energy of the pristine ZnO surface. To compare the formation energies of different defects, we used the chemical potential of oxygen in the gas phase to align the environmental effects. μ_O^θ is the standard chemical potential of O, and R, T, and p represent the ideal gas constant, temperature, and the partial pressure of O_2, respectively. Secondly, the Zn–O dimer vacancy formation energy $\left(E_f^{(Zn-O)_{DiV}}\right)$ was calculated as:

$$E_f^{(Zn-O)_{DiV}} = E_{slab}^{(Zn-O)_{DiV}} + E_{bulk}^{ZnO} - E_{slab}^{pristine} \tag{4}$$

where $E_{slab}^{(Zn-O)_{DiV}}$ is the total energy of the surface with a Zn–O dimer vacancy, and E_{bulk}^{ZnO} is obtained by calculating the energy of a 'Zn–O' group in the bulk wurtzite-ZnO. Notably, we can find that the formation energy of the Zn–O dimer vacancy is constant

under various conditions of oxygen potential. Finally, the zinc vacancy formation energy ($E_f^{Zn_V}$) was calculated according to

$$E_f^{Zn_V} = E_{slab}^{Zn_V} + E_{bulk}^{ZnO} - \frac{1}{2}E_{mol}^{O_2} - E_{slab}^{pristine} - \Delta\mu_O \qquad (5)$$

where $E_{slab}^{Zn_V}$ is the total energy of the surface with a single zinc vacancy.

Notably, the choice for the size of the slab model has been systematically tested by the formation energy of different defects (Fig. S1†), and it was found that the formation energies of the various types of surface defects (O_V and $(Zn-O)_{Div}$) largely converged with the size above $p(4 \times 3)$ ($\theta = 1/12$ ML), which is also in agreement with previous reports.[28,29]

Results and discussion

Pristine and defect ZnO(10$\bar{1}$0) surfaces

The {10$\bar{1}$0} facet is the most stable one for ZnO in the hexagonal wurtzite phase.[35] The surface Zn and O atoms on the ZnO(10$\bar{1}$0) surface are three-fold coordinated (denoted as Zn_{3c} and O_{3c}), while the Zn and O atoms in the subsurface and bulk region are four-fold coordinated (denoted as Zn_{4c} and O_{4c}). The exposed surface Zn–O pairs can be recognized as the Zn–O dimer and Zn–O trench, as shown in Fig. 1a. When an O or Zn atom or Zn–O dimer is removed from the surface, the coordination number of the surface/subsurface Zn/O around the vacancy is reduced to

2 or 3. Considering that under real reaction conditions, the ZnO surface may have these different forms of defects,[28,36] *i.e.*, zinc vacancy (denoted as Zn_V), Zn–O dimer vacancy (denoted as $(Zn-O)_{Div}$, see Fig. 1b) and oxygen vacancy (denoted as O_V, see Fig. 1c), we first systematically investigated their relative stabilities by calculating the formation energies of different defect ZnO(10$\bar{1}$0) surfaces with respect to the oxygen chemical potentials ($\Delta\mu_O$) ($E_f - \Delta\mu_O$, Fig. S2†). The plotted equilibrium phase diagrams of these surfaces under different (p_{CO_2}/p_{CO}) and T (Fig. 1d) showed that, consistent with the previously reported stable structures,[34] both $(Zn-O)_{Div}$ and O_V surfaces (ZnO(10$\bar{1}$0)–$(Zn-O)_{Div}$ and ZnO(10$\bar{1}$0)–O_V, see Fig. 1b and c) can occur favorably under reaction conditions ($T = 400$–900 K, (p_{CO_2}/p_{CO}) = 10^{-3}–10^3).[37,38] The $(Zn-O)_{Div}$ is relatively more likely to form under atmospheric CO_2/CO pressure ratio ((p_{CO_2}/p_{CO}) ~ 10^3, with the corresponding O_2 partial pressure being 0.2 bar). In addition, it needs to be noted that the formation of an O vacancy will leave 2 excess electrons in the ZnO(10$\bar{1}$0)–O_V system (Fig. 1c), which could help the adsorption of electrophilic species and its transformation into negatively charged species (such as the hydride).[39,40] When the Zn–O dimer vacancy occurs, the ZnO(10$\bar{1}$0)–$(Zn-O)_{Div}$ surface remains charge balanced, though this defect surface obviously becomes more open for the adsorption and activation of relevant reactants.

We also investigated the electronic properties of the pristine and various defect ZnO(10$\bar{1}$0) surfaces by calculating the density
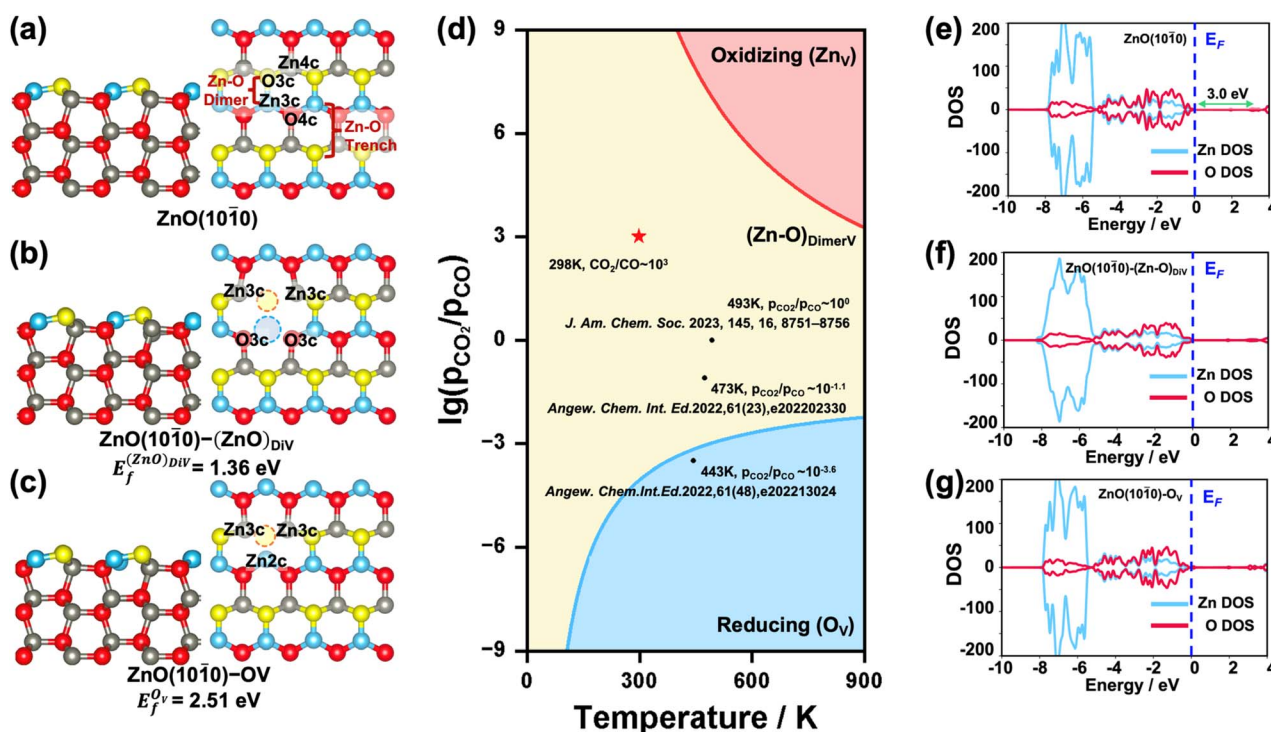

Fig. 1 (a–c) Calculated structures of pristine and various defect ZnO(10$\bar{1}$0) surfaces, and coordinate numbers of surface/subsurface atoms around defects. Left: side view, right: top view. Blue and yellow spheres represent surface Zn and O atoms, and grey and red spheres represent subsurface Zn and O atoms, while dotted lines of blue and red represent Zn and O vacancies, respectively. (d) Calculated lg(p_{CO_2}/p_{CO})–T phase diagrams of different defect ZnO(10$\bar{1}$0) surfaces; red star denotes normal temperature and atmospheric conditions, and black dots denote some reported conditions of relevant reactions catalyzed by ZnO. (e–g) Calculated DOS of (e) pristine and (f and g) defect ZnO(10$\bar{1}$0) surfaces. All DOS are aligned with respect to the Fermi energy level (E_F). These notations are used throughout this paper.

of states (DOS) (Fig. 1e–g). The calculated band gap of the pristine ZnO(10$\bar{1}$0) surface was 3.0 eV, which largely agrees with the experimental result (3.3 eV).[41] Further analysis of the partial DOS (pDOS) showed that most of the Zn 3d electrons lay deeply below the Fermi energy level (E_F), clearly caused by the fully filled orbitals with strong correlations,[42] and it also hints at a unique bonding pattern with other species. Besides, from the calculated DOS of the defect surface, we can clearly see that the bonding symmetry change caused by the Zn–O dimer vacancy also has a strong influence on the shape of Zn 3d orbitals (Fig. 1f and S2a†), which are broadened obviously. By contrast, the excess electrons contributed by the O vacancy do shrink the unoccupied dsp hybrid orbital (Fig. S3a†), but they do not change the shape of the Zn orbitals or bring about a new electronic state under E_F, indicating a new way of storing electrons that is different from that of some reducible metal oxides,[43,44] whose extra electrons would be localized at specific atomic orbitals. In fact, we have also determined that when the 2 electrons resulting from the formation of an oxygen vacancy are forced to be localized at the oxygen vacancy site, the corresponding vacancy formation energy is 0.70 eV higher than that when the 2 electrons are delocalized in the system (Fig. 2c and S3b†); and the pDOS calculation (Fig. S3b†) suggested that these excess electrons would exist within the hybrid orbitals throughout the ZnO bulk, just like the electrons from other atoms. Thus, the Zn orbitals appear to be rather flexible for electron storage.

Adsorption of a single H atom on different ZnO(10$\bar{1}$0) surfaces

Previous studies showed that the hydride species is key to the CO/CO$_2$ selective hydronation at metal oxides.[45,46] To determine if one H adsorbed on the ZnO(10$\bar{1}$0), ZnO(10$\bar{1}$0)–O$_V$ and ZnO(10$\bar{1}$0)–(Zn–O)$_{DiV}$ surfaces can form a proton (H$^+$), hydride (H$^-$) or H radical (H$^•$), we performed the Bader charge analysis

and calculated the corresponding spin charge density differences (Fig. 2 and S3†). Notably, the hydride species does not show net spin density, while for the H radical, it usually possesses a net spin density with the calculated Bader charge close to zero.

Firstly, we calculated the adsorption of one H atom at O sites on these surfaces. The calculated results showed that one electron from the H would preferentially transfer to the pristine and different defect ZnO(10$\bar{1}$0) surfaces (Fig. S4†), and the corresponding Bader charges are +0.62, +0.63 and +0.66 |e| for the adsorbed H on the pristine, (Zn–O)$_{DiV}$ and O$_V$ surfaces, respectively, indicating that the proton species are formed. The calculated results also showed that the adsorption of the H atom at the O$_{3c}$ site on the ZnO(10$\bar{1}$0)–(Zn–O)$_{DiV}$ surface is exothermic by 1.28 eV. Such a favorable adsorption can be due to the fact that the adsorption location is rather open and the adsorbed H species can form the hydrogen bond with the neighboring O$_{3c}$ (the distance between O$_{3c}$ and H atoms is 2.05 Å, Fig. S4d†). The adsorption of one H atom at the O$_{3c}$ site on the ZnO(10$\bar{1}$0)–O$_V$ surface was calculated to be exothermic by 0.71 eV only. This is mainly because the presence of the two excess electrons on the reduced ZnO(10$\bar{1}$0) surface further increases the electron repulsion within the system. Notably, we can also find that the extra electron from an adsorbed H (Fig. S4c, f and i†) barely has any influence on the overall shape of the Zn orbitals of the various ZnO(10$\bar{1}$0) surfaces, which again suggests the flexibility of Zn orbitals in storing electrons.

In addition, we also calculated the adsorption of one H atom at Zn sites on these surfaces. The results showed that the H species, as a radical, is barely adsorbed at the Zn site on the ZnO(10$\bar{1}$0) surface since the adsorption is endothermic by 1.48 eV (Fig. 2a and d). By contrast, the H adsorbed on the ZnO(10$\bar{1}$0)–O$_V$ surface can actually form three H–Zn bonds at the O$_V$ site, and it turns into a hydride species (Fig. 2c, the
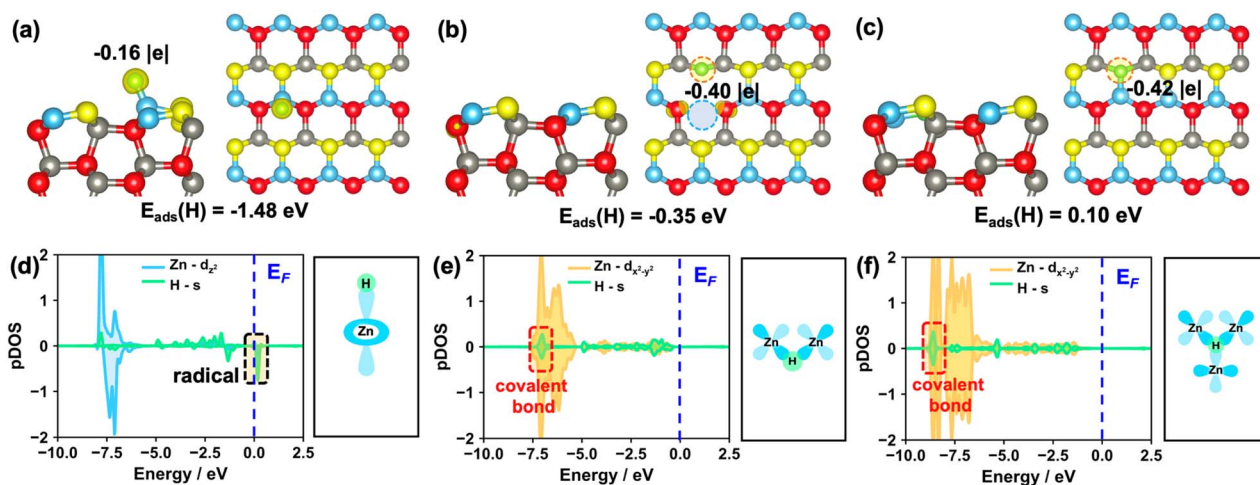

Fig. 2 (a–c) Calculated structures and energies of the single H atom adsorption at the surface/subsurface Zn sites of pristine and various defect ZnO(10$\bar{1}$0) surfaces. Calculated Bader charges of H and spin charge density differences are also shown. The spin iso-surfaces (yellow) are plotted at a value of 0.05 e Å^{-3}, this notation is used throughout the paper. Green: H atoms. (d–f) Calculated partial DOS (pDOS) of the adsorbed H and corresponding Zn on the pristine and defect ZnO(10$\bar{1}$0) surfaces. E_F is labelled with dashed blue lines, and all pDOS are aligned with respect to the E_F.

corresponding Bader charge is $-0.42\ |e|$) with the exothermic adsorption energy of 0.10 eV. This result is largely consistent with the findings that the hydride species can form on some reduced metal oxide surfaces such as CeO_2.[39,45] For the adsorption of a single H atom at the Zn site on the $ZnO(10\bar{1}0)$–$(Zn–O)_{DiV}$ surface, the hydride, rather than a H radical, is also formed (Fig. 2b, the calculated Bader charge is $-0.40\ |e|$), though this process is endothermic by 0.35 eV. In this case, the adsorbed H species would interact with the two Zn_{3c} (Fig. 2e). Notably, the electronic analysis suggested that the hydrides on both the O_V and $(Zn–O)_{DiV}$ surfaces occur *via* the covalent bonds contributed by the s electron from H and the multiple symmetric d electrons from Zn, in particular $d_{x^2-y^2}$ (Fig. 2e and f), and the energy levels of the as-formed covalent Zn–H bonds at $ZnO(10\bar{1}0)$–$(Zn–O)_{DiV}$ and $ZnO(10\bar{1}0)$–$(Zn–O)_{OV}$ are far below E_F.

H_2 dissociation on different $ZnO(10\bar{1}0)$ surfaces

In real applications, the hydride species for selective hydrogenation reactions usually come from the dissociation of H_2 molecules on the catalysts.[42,47] Accordingly, we also systematically studied the possible pathways of the dissociative adsorption of H_2 on the pristine and various defect $ZnO(10\bar{1}0)$ surfaces (Fig. 3, S5 and S6†), including the homolytic dissociation at (i) two O sites to produce two hydroxyl (O–H) groups or (ii) two Zn sites to produce two Zn–H species, as well as (iii) the heterolytic dissociation at the Zn and O sites for the formation of Zn–H and O–H species.

The calculated results showed that the homolytic dissociation of H_2 to form two O–H species at O sites on the pristine, Zn–O dimer vacancies and oxygen vacancies of the $ZnO(10\bar{1}0)$ surfaces needs to overcome the energy barriers of 1.48 eV,

0.70 eV and 1.52 eV (Fig. 3a and S6b, e and h†), respectively, and they are exothermic by 0.64 eV, 1.57 eV and 0.98 eV (Fig. 3a, c, f and i), respectively. Our results also showed that the homolytic H_2 dissociation can produce two Zn–H species at adjacent Zn_{3c} sites on the $ZnO(10\bar{1}0)$, $ZnO(10\bar{1}0)$–$(Zn–O)_{DiV}$ and $ZnO(10\bar{1}0)$–O_V surfaces, and the corresponding electronic analyses indicated that they are 2Zn–H·, Zn–H· and Zn–H⁻, and O_V–H⁻ and Zn–H⁻ species, respectively. Moreover, these processes need to overcome energy barriers as high as 2.81 eV, 2.38 eV and 1.43 eV, respectively (Fig. 3a and S6c, f and i†), and the calculated reaction energies also indicated that these processes are energetically unfavorable.

On the other hand, according to our calculated results, the heterolytic H_2 dissociation on the different ZnO surfaces ($ZnO(10\bar{1}0)$, $ZnO(10\bar{1}0)$–$(Zn–O)_{DiV}$ and $ZnO(10\bar{1}0)$–O_V surfaces) can readily occur to form the Zn–H⁻ and O–H species, which only need to overcome the small energy barriers of 0.45 eV, 0.10 eV and 0.45 eV (Fig. 3a and S6a, d and g†), respectively, and the corresponding processes are exothermic by 0.53 eV, 1.51 eV and 0.77 eV, which are consistent with those reported in previous experimental and theoretical studies.[20,48,49] The stabilities could be attributed to the structural features of the transition states of the heterolytic H_2 dissociations: the characteristic [H–O–Zn–H] four-membered ring at $ZnO(10\bar{1}0)$, the [H–O–Zn–O–Zn–H] hexatomic ring at $ZnO(10\bar{1}0)$–$(Zn–O)_{DiV}$ and a double [H–O–Zn–O–Zn–H] hexatomic ring at $ZnO(10\bar{1}0)$–O_V.

From the above results, we can find that H_2 can be activated more readily through heterolytic dissociation rather than homolytic cleavage on the different ZnO surfaces, which is also consistent with the previously reported results on some other metal oxides.[18,20,50] Specifically, among the different $ZnO(10\bar{1}0)$ surfaces, the $(Zn–O)_{DiV}$ surface is the most active one for the
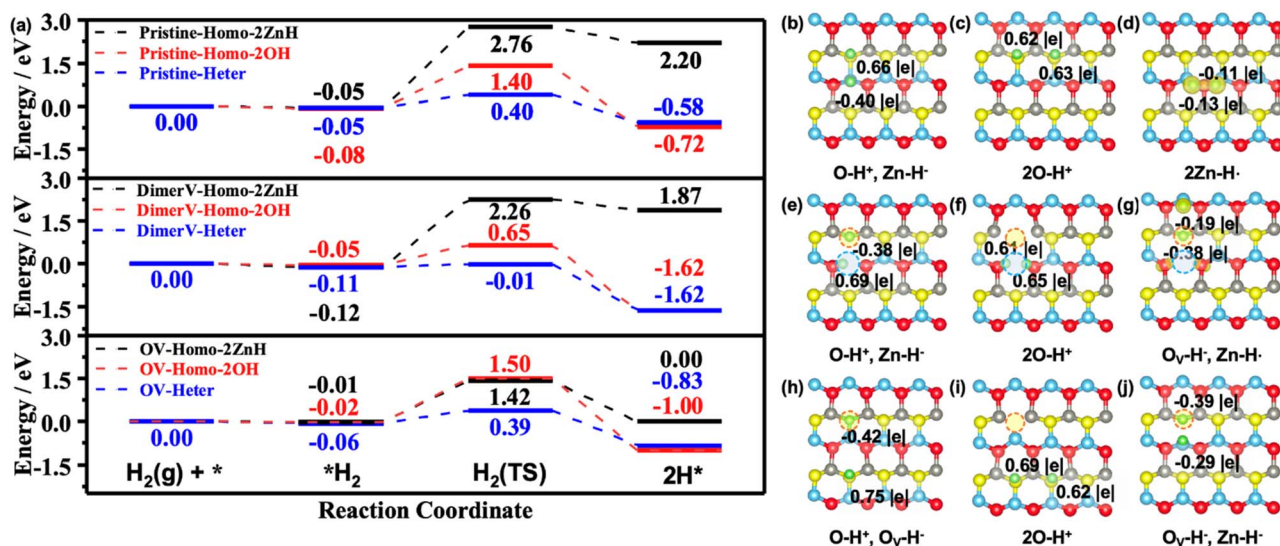

Fig. 3 (a) Calculated energy profiles of H_2 adsorption and dissociation on the pristine and various defect $ZnO(10\bar{1}0)$ surfaces. $H_2(g)$, $*H_2$, $H_2(TS)$, and 2H* represent the states of gas-phase H_2, surface adsorbed H_2, transition state for the surface adsorbed H_2 to dissociate into two surface adsorbed H, and co-adsorption of two H species, respectively. (b–j) Calculated structures (top view) of the products of H_2 dissociation on the pristine and defect $ZnO(10\bar{1}0)$ surfaces, and the calculated Bader charges and spin charge densities of the co-adsorption of two H species are also shown.

heterolytic H_2 dissociation. This is because the low-coordinated O species around the Zn_V site on the $ZnO(10\bar{1}0)$–$(Zn$–$O)_{DiV}$ surface are rather active for the transformation of the adsorbed H into stable protons, while the O_V site on the $(Zn$–$O)_{DiV}$ surface can help produce the stable hydrides that interact with the surface through covalent Zn–H bonds. We also performed the density-functional perturbation theory (DFPT) calculations[51,52] of the O–H and Zn–H species produced by the heterolytic H_2 dissociation on the $ZnO(10\bar{1}0)$ and $ZnO(10\bar{1}0)$–$(Zn$–$O)_{DiV}$ surfaces, and obtained the corresponding simulated infrared (IR) spectra (3550 (O–H) and 1773 (Zn–H) cm^{-1} for pristine $ZnO(10\bar{1}0)$; 3345 (O–H) and 1522 (Zn–H) cm^{-1} for $ZnO(10\bar{1}0)$–$(Zn$–$O)_{DiV}$; see Fig. S7†). The wavenumber differences for the species on the pristine and $(Zn$–$O)_{DiV}$ surfaces are due to their different structures, i.e. on the $(Zn$–$O)_{DiV}$ surface, the O–H species can also form a hydrogen bond with the neighboring lattice O, and the hydride actually bonds with two Zn sites. These calculated wavenumbers are largely consistent with the reported experimental results that the pristine $ZnO(10\bar{1}0)$ surface gives rise to 3490 (O–H) and 1710 (Zn–H) cm^{-1} and the $ZnO(10\bar{1}0)$–$(Zn$–$O)_{DiV}$ gives rise to 3400 (O–H) and 1475 (Zn–H) cm^{-1}.[48,53,54]

Besides, to further understand the energy barrier and product stability of heterolytic H_2 dissociation on the different surfaces, we also calculated the partial DOS of the H species in the transition and final states of these processes (Fig. 4, S8 and S9†). The results indicated that the Zn–H ionic bonds occur in the transition states on the $ZnO(10\bar{1}0)$ and $ZnO(10\bar{1}0)$–O_V surfaces (Fig. 4a). Moreover, the structural properties of the Zn–H bonds in the transition states (Fig. S8†) also showed that only a single asymmetric Zn–H bond forms on the pristine and O_V

surfaces, while the double symmetric Zn–H bond occurs on the $(Zn$–$O)_{DiV}$ surface. Accordingly, higher energy barriers were obtained on the pristine and O_V surfaces (0.45 eV) compared with that on the $(Zn$–$O)_{DiV}$ surface (0.10 eV). Interestingly, stable covalent Zn–H bonds with relatively low energy levels can be formed on the defect surfaces, while Zn–H ionic bonds with relatively high energy levels were formed on the pristine $ZnO(10\bar{1}0)$ surface, leading to the different stabilities of the hydride species on the three surfaces.

The corresponding Bader charge and spin charge density difference analyses (Fig. 3b–j) also supported that the heterolytic H_2 dissociation on the various surfaces indeed produced a hydride and a hydroxyl species. The calculated Bader charges of the formed H^+ and H^- species are +0.66 $|e|$ and −0.40 $|e|$ at $ZnO(10\bar{1}0)$, +0.69 $|e|$ and −0.38 $|e|$ at $ZnO(10\bar{1}0)$–$(Zn$–$O)_{DiV}$, and +0.75 $|e|$ and −0.42 $|e|$ at $ZnO(10\bar{1}0)$–O_V. Interestingly, one can notice that the value of the calculated charge of H^+ is approximately two times that of H^- on the different $ZnO(10\bar{1}0)$ surfaces. This suggested that only some part of the charge contributed by the H during H_2 dissociation is used to activate another H to form the hydride species, while the other part of the charge might be transferred to the $ZnO(10\bar{1}0)$ surface (Table S2†). This is very different from some other metal oxides (e.g., MgO and CeO_2), on which the calculated Bader charges of the H^+ and H^- species generated through heterolytic H_2 dissociation are approximately equal.[45,55]

For this unusual phenomenon, the calculated DOS (Fig. S8†) of the products of heterolytic H_2 dissociation showed that the shapes of the Zn orbitals are almost unchanged, which is consistent with the situations of single H adsorption at surface O explored earlier on. In fact, the hydrides from these heterolytically dissociated H_2 molecules can be recognized to evolve from the H adsorbing immediately following the H^+ formation at the surface O site, in which case the electrons are released after storage. Therefore, it can also be concluded that the Zn orbitals are indeed quite flexible since they largely maintain the same shape during electron storage/release.

Finally, we further investigated if the transferred charge from the adsorbed H can be involved in the generation of multiple hydrides on the $ZnO(10\bar{1}0)$–$(Zn$–$O)_{DiV}$ surface (Fig. 5). The calculated results showed that, together with the surface H^+, two hydride species can indeed occur, and their corresponding Bader charges are −0.36 $|e|$ and −0.31 $|e|$ (Fig. 5a). However, the charge contributed by one adsorbed H species
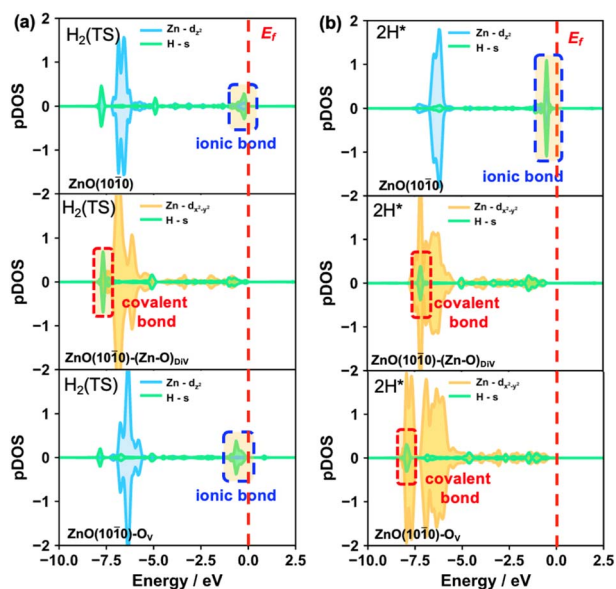

Fig. 4 Calculated partial DOS of the adsorbed H species at Zn or O_V sites and the interacting Zn. The results for the (a) transition and (b) final states of heterolytic H_2 dissociation on the pristine and various defect $ZnO(10\bar{1}0)$ surfaces. E_F is labelled by red dashed lines, and all pDOS are aligned with respect to the E_F.
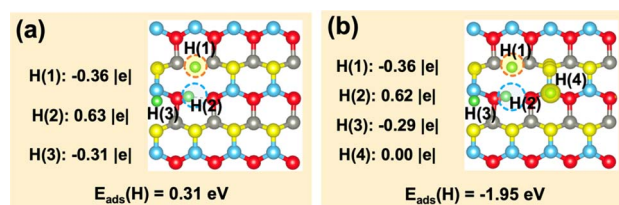

Fig. 5 Calculated adsorption energies and structures of co-adsorption of one $H^+ + 2H^-$ and $H^+ + 2H^- + H^·$. (a) H^+ co-adsorption with $2H^-$. (b) H^+ co-adsorption with $2H^-$ and one $H^·$. Calculated Bader charge values of H and spin charge density differences are also shown.

cannot be used to activate more adsorbed H to the hydride species (*e.g.*, the corresponding Bader charges of the three co-adsorbed H species are −0.36, −0.29 and 0.00 |*e*|, respectively, forming only two hydride species; Fig. 5b). Thus, we can expect that the charge released by the formation of a proton may perform dual functions for the simultaneous activation of two electrophilic adsorbates (*e.g.*, $CO_2^{\delta-}$ and hydride).

Selective CO_2 hydrogenation on pristine and various defect $ZnO(10\bar{1}0)$ surfaces

To unveil the catalytic reactivities of the hydride species, we then proceeded to investigate the CO_2 activation and hydrogenation on the $ZnO(10\bar{1}0)$, $ZnO(10\bar{1}0)$–O_v and $ZnO(10\bar{1}0)$–$(Zn–O)_{DiV}$ surfaces (Fig. 6 and S10–S19†). It is well known that the adsorption and activation of CO_2 are the key steps of the overall CO_2 reduction reactions.[56,57] Our calculated results showed that the CO_2 adsorptions on the $ZnO(10\bar{1}0)$, $ZnO(10\bar{1}0)$–O_v and $ZnO(10\bar{1}0)$–$(Zn–O)_{DiV}$ surfaces all lead to the formation of carbonate (CO_3^{2-})-like species, and these processes are exothermic by 1.01 eV, 0.98 eV and 1.03 eV, respectively (Fig. 6a). The Bader charge analysis also showed that the adsorbed CO_2 is negatively charged on these surfaces (the corresponding Bader charges are −0.20 |*e*|, −0.22 |*e*| and −0.21 |*e*|, respectively (see Fig. 6b–d)).

Next, we calculated the further adsorption of H_2 and found that it is generally rather weak on the pristine and different defect $ZnO(10\bar{1}0)$ surfaces with the pre-adsorbed CO_2 (the corresponding adsorption energies are close to 0 eV; see Fig. 6a and S11†). The adsorbed H_2 then undergoes heterolytic dissociation to produce one hydride and one proton species with the barriers of 0.49 eV, 0.30 eV and 0.42 eV on the pristine and defect

$ZnO(10\bar{1}0)$ surfaces, and the corresponding processes are exothermic by 0.53 eV, 1.69 eV and 0.77 eV. Interestingly, we also found that the adsorption energies of CO_2 were enhanced by 0.18 eV and 0.06 eV on the pristine and $(Zn–O)_{DiV}$ surfaces, respectively, following the heterolytic dissociation of the H_2, in comparison with the CO_2 adsorbed alone. This is consistent with our findings above that the charges provided by the H that turns into a proton have 'dual functions' in activating multiple adsorbates.

We next considered two possible routes for CO_2 activation, *i.e.* direct dissociation of CO_2 and direct hydrogenation of CO_2. The results indicated that the direct CO_2 dissociation into co-adsorbed *CO and *O on the $ZnO(10\bar{1}0)$, $ZnO(10\bar{1}0)$–$(Zn–O)_{DiV}$ and $ZnO(10\bar{1}0)$–O_v surfaces requires endothermic energies of 5.09 eV, 5.04 eV and 4.78 eV (Fig. S12†), respectively, and such high energy demands suggested that direct CO_2 dissociation is unfavorable. In the route of direct hydrogenation of CO_2, two possible pathways were then tested (Fig. 6 and S13–S15†). The first is the so-called COOH (carboxyl) pathway, in which the H^+ or H^- binds with the $O^{\delta-}$ of the adsorbed CO_2 to form a *COOH species; the second is the so-called HCOO (formate) pathway, in which the H^+ or H^- reacts with the $C^{\delta+}$ of the adsorbed CO_2 to produce a *HCOO species. According to our calculated results, the processes with the H^+ attacking the adsorbed CO_2 to form the *HCOO species need to overcome enormously large energy barriers of 4.29 eV, 2.76 eV and 6.42 eV on the $ZnO(10\bar{1}0)$, $ZnO(10\bar{1}0)$–O_v and $ZnO(10\bar{1}0)$–$(Zn–O)_{DiV}$ surfaces, respectively, and they are also highly endothermic (4.13 eV, 1.92 eV and 4.13 eV, respectively; Fig. S13a, e and i, and S14a, e and i†). When the H^+ species attacks the $O^{\delta-}$ of the adsorbed CO_2 to generate a *COOH species (Fig. S13c, g, and k, and S14c, g and
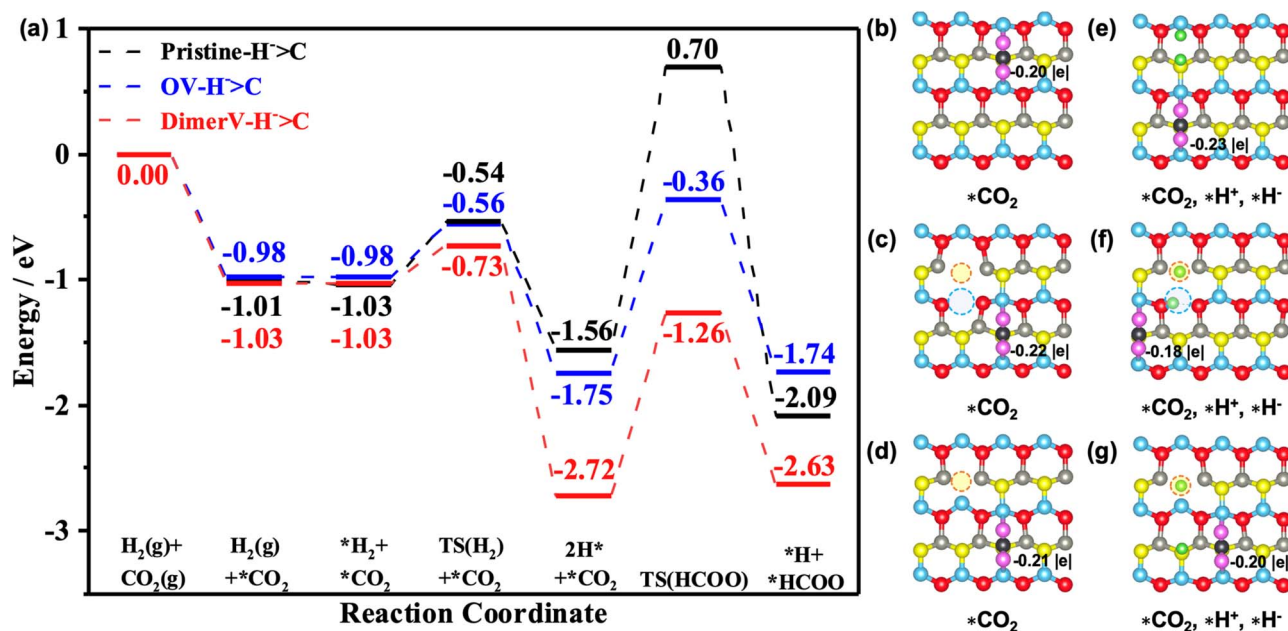

Fig. 6 (a) Calculated energy profiles of the most favorable routes of selective CO_2 hydrogenation on the pristine and defect $ZnO(10\bar{1}0)$ surfaces. (b–d) Calculated structures (top view) of CO_2 adsorption and (e–g) co-adsorption with heterolytically dissociated H_2 on the pristine and defect $ZnO(10\bar{1}0)$ surfaces. Black: C atoms, pink: O atoms of CO_2. Calculated Bader charges of CO_2 species are also shown.

k†), it also needs to overcome very large energy barriers (4.25 eV, 1.43 eV and 4.06 eV on the $ZnO(10\bar{1}0)$, $ZnO(10\bar{1}0)$–O_v and $ZnO(10\bar{1}0)$–$(Zn-O)_{DiV}$ surfaces, respectively) and these processes are highly endothermic (1.05 eV, 1.02 eV and 1.34 eV). Interestingly, for the processes with the H^- species as the active H species to react with CO_2, both the carboxylate and formate pathways can occur quite easily. For the pathway for the hydride species to attack the $C^{\delta+}$ of the adsorbed CO_2 to form the *HCOO species, the energy barriers are 2.26 eV, 1.39 eV and 1.46 eV on the pristine and the two defect $ZnO(10\bar{1}0)$ surfaces and they are exothermic by 0.53 eV and endothermic by 0.01 eV and 0.09 eV, respectively. At the same time, the reactions between H^- and the $O^{\delta-}$ of the adsorbed CO_2 (the COOH pathway) need to overcome the energy barriers of 2.42 eV, 1.40 eV and 1.71 eV, while they are endothermic by 0.09 eV, 0.05 eV and 0.67 eV.

In addition, we also calculated the subsequent hydrogenation reaction steps in both the HCOO-to-methanol pathway and the COOH-to-methanol pathway (Fig. S16–19†) on the $ZnO(10\bar{1}0)$–$(ZnO)_{DiV}$ surface. The results indicated that the HCOO-to-methanol pathway is more favorable than the COOH-to-methanol pathway in the formation of *H_2CO species, where the maximum endothermic step (*HCOO + *H^- → *HCOOH, $\Delta E = 0.78$ eV) of the HCOO-to-methanol pathway is lower than that of the COOH-to-methanol pathway (*CO + *OH + *H^+ → *CO + H_2O(g), $\Delta E = 1.29$ eV) (Fig. S16 and S18†). After the formation of the *H_2CO species, the H_2 dissociation into H^+ and H^- species releases an exothermic energy of 0.56 eV, while the formation of *H_3CO is exothermic by 1.67 eV. The subsequent step of H_2 adsorption and dissociation is exothermic by 0.18 eV, and the formation of *CH_3OH species is highly exothermic by 1.89 eV. Therefore, it can be concluded that the *HCOO species is more readily formed and more stable during the CO_2 hydrogenation to methanol reaction, and we believe that the *HCOO intermediate species is the most abundant reactive intermediate (MARI) in the CO_2 hydrogenation reaction, which is consistent with other reports.[58,59]

From the above results, one can surely expect that the CO_2 hydrogenation with the H^- species on the $ZnO(10\bar{1}0)$–$(Zn-O)_{DiV}$ surface is more likely to follow the HCOO pathway, which may lead to the formation of CH_3OH as the main product,[60] and this stoichiometric surface with $(Zn-O)_{DiV}$ defects is more active than the reduced one with O_V defects. This result is consistent with those reported recently by Ling et al.[17] Moreover, the simulated infrared spectra (calculated by the DFPT method[51,52]) of formate (1355 and 1515 cm^{-1}, Fig. S20†) are also consistent with the reported experimental results[61,62] (1370 and 1595 cm^{-1}). In general, we can learn from the calculated results in the current work that defects on the $ZnO(10\bar{1}0)$ surface are key to its improved catalytic activities in H_2 activation and CO_2 hydrogenation, and the Zn–O dimer vacancy appears even more active than the usual O vacancy.

Conclusions

In summary, this study has systematically explored the catalytic roles of ZnO in CO_2 hydrogenation to methanol, with a particular focus on the generation of active hydrogen species and their impact on catalysis. Our comprehensive computational analyses, based on density functional theory, have revealed the unique electronic properties of ZnO and their substantial influence on the catalytic processes. The characteristic $ZnO(10\bar{1}0)$, $ZnO(10\bar{1}0)$–O_V and $ZnO(10\bar{1}0)$–$(Zn-O)_{DiV}$ surfaces were constructed, and their stabilities were verified with the calculated equilibrium phase diagrams under reaction conditions. The calculated DOS further showed that for the pristine and various defect $ZnO(10\bar{1}0)$ surfaces, the size of the unfilled hybrid orbitals changes while the shape of the occupied orbitals remains unchanged when excess electrons exist, revealing the unique way of storing electrons for ZnO. We also determined that the hydride species can form through heterolytic H_2 dissociation on the pristine and various defect $ZnO(10\bar{1}0)$ surfaces. Among these surfaces, the $ZnO(10\bar{1}0)$–$(Zn-O)_{DiV}$ is the most active one for the heterolytic dissociation of H_2, which demonstrates a notably low energy barrier (~0.10 eV), largely due to the fact that the low-coordinated surface Zn_{3c} is helpful for the stabilization of H^- species. Moreover, it was found that the unique way of storing and releasing electrons in Zn orbitals gives ZnO the characteristic capacity of activating two electrophilic adsorbates simultaneously as excess electrons exist. Calculations of the key reaction steps further showed that the covalent Zn–H species can regulate the activities and selectivities in CO_2 hydrogenation, by preferentially producing *HCOO intermediates, and revealed a lower reaction barrier on the Zn–O dimer vacancy surface. Our study provides valuable insights into the catalytic mechanisms of ZnO in hydrogenation reactions, highlighting the importance of its surface structures and electronic properties, and suggests the potential of the $(Zn-O)_{DiV}$-containing ZnO surface as an efficient catalyst for hydrogenation reactions.

Data availability

The data supporting this article have been included in the main article and the ESI.†

Author contributions

X.-Y. Z. performed the DFT calculations, and collected and analyzed the DFT data. Z.-Q. W. supervised the research, analyzed the DFT data and provided constructive suggestions. X.-Q. G. conceived the ideas, supervised the research, and designed the present work. All authors contributed to the discussion and the manuscript writing.

Conflicts of interest

The authors declare no conflicts of interest.

Acknowledgements

References

1 G. Ertl, H. Knözinger and J. Weitkamp, *Handbook of Heterogeneous Catalysis*, VCH, 1997.

2 G. A. Olah, A. Goeppert and G. K. S. Prakash, *Beyond Oil and Gas: The Methanol Economy*, John Wiley & Sons, 2018.

3 M. Behrens, *J. Catal.*, 2009, **267**, 24–29.

4 S. A. Kondrat, P. J. Smith, P. P. Wells, P. A. Chater, J. H. Carter, D. J. Morgan, E. M. Fiordaliso, J. B. Wagner, T. E. Davies, L. Lu, J. K. Bartley, S. H. Taylor, M. S. Spencer, C. J. Kiely, G. J. Kelly, C. W. Park, M. J. Rosseinsky and G. J. Hutchings, *Nature*, 2016, **531**, 83–87.

5 X. Liu, J. Luo, H. Wang, L. Huang, S. Wang, S. Li, Z. Sun, F. Sun, Z. Jiang, S. Wei, W.-X. Li and J. Lu, *Angew. Chem., Int. Ed.*, 2022, **61**, e202202330.

6 P. Amann, B. Klötzer, D. Degerman, N. Köpfle, T. Götsch, P. Lömker, C. Rameshan, K. Ploner, D. Bikaljevic, H.-Y. Wang, M. Soldemo, M. Shipilin, C. M. Goodwin, J. Gladh, J. Halldin Stenlid, M. Börner, C. Schlueter and A. Nilsson, *Science*, 2022, **376**, 603–608.

7 S. Kuld, M. Thorhauge, H. Falsig, C. F. Elkjær, S. Helveg, I. Chorkendorff and J. Sehested, *Science*, 2016, **352**, 969–974.

8 I. Kasatkin, P. Kurr, B. Kniep, A. Trunschke and R. Schlögl, *Angew. Chem., Int. Ed.*, 2007, **46**, 7324–7327.

9 M. Behrens, F. Studt, I. Kasatkin, S. Kühl, M. Hävecker, F. Abild-Pedersen, S. Zander, F. Girgsdies, P. Kurr, B.-L. Kniep, M. Tovar, R. W. Fischer, J. K. Nørskov and R. Schlögl, *Science*, 2012, **336**, 893–897.

10 S. Kattel, P. J. Ramírez, J. G. Chen, J. A. Rodriguez and P. Liu, *Science*, 2017, **355**, 1296–1299.

11 Y. Wang, S. Kattel, W. Gao, K. Li, P. Liu, J. G. Chen and H. Wang, *Nat. Commun.*, 2019, **10**, 1166.

12 W. Wu, Y. Wang, L. Luo, M. Wang, Z. Li, Y. Chen, Z. Wang, J. Chai, Z. Cen, Y. Shi, J. Zhao, J. Zeng and H. Li, *Angew. Chem., Int. Ed.*, 2022, **61**, e202213024.

13 Y.-F. Shi, P.-L. Kang, C. Shang and Z.-P. Liu, *J. Am. Chem. Soc.*, 2022, **144**, 13401–13414.

14 J. C. Frost, *Nature*, 1988, **334**, 577–580.

15 H. Shi, H. Yuan, Z. Li, W. Wang, Z. Li and X. Shao, *J. Phys. Chem. C*, 2019, **123**, 13283–13287.

16 M. Buchholz, P. G. Weidler, F. Bebensee, A. Nefedov and C. Wöll, *Phys. Chem. Chem. Phys.*, 2014, **16**, 1672–1678.

17 Y. Ling, J. Luo, Y. Ran, Z. Liu, W.-X. Li and F. Yang, *J. Am. Chem. Soc.*, 2023, **145**, 22697–22707.

18 B. Song, Y. Li, X.-P. Wu, F. Wang, M. Lin, Y. Sun, A. Jia, X. Ning, L. Jin, X. Ke, Z. Yu, G. Yang, W. Hou, W. Ding, X.-Q. Gong and L. Peng, *J. Am. Chem. Soc.*, 2022, **144**, 23340–23351.

19 Q.-L. Tang and Q.-H. Luo, *J. Phys. Chem. C*, 2013, **117**, 22954–22966.

20 J. Luo, J.-X. Liu and W.-X. Li, *J. Phys. Chem. C*, 2022, **126**, 9059–9068.

21 Y.-F. Zhao, R. Rousseau, J. Li and D. Mei, *J. Phys. Chem. C*, 2012, **116**, 15952–15961.

22 W. Tu, P. Ren, Y. Li, Y. Yang, Y. Tian, Z. Zhang, M. Zhu, Y.-H. C. Chin, J. Gong and Y.-F. Han, *J. Am. Chem. Soc.*, 2023, **145**, 8751–8756.

23 G. Kresse and J. Furthmüller, *Phys. Rev. B: Condens. Matter Mater. Phys.*, 1996, **54**, 11169–11186.

24 P. E. Blöchl, *Phys. Rev. B: Condens. Matter Mater. Phys.*, 1994, **50**, 17953–17979.

25 J. P. Perdew, K. Burke and M. Ernzerhof, *Phys. Rev. Lett.*, 1996, **77**, 3865–3868.

26 M. P. Teter, M. C. Payne and D. C. Allan, *Phys. Rev. B: Condens. Matter Mater. Phys.*, 1989, **40**, 12255–12263.

27 R. Escudero and R. Escamilla, *Solid State Commun.*, 2011, **151**, 97–101.

28 Y. Cao, J. Luo, W. Huang, Y. Ling, J. Zhu, W.-X. Li, F. Yang and X. Bao, *J. Chem. Phys.*, 2020, **152**, 074714.

29 K. Mun Wong, S. M. Alay-e-Abbas, A. Shaukat, Y. Fang and Y. Lei, *J. Appl. Phys.*, 2013, **113**, 014304.

30 J. Heyd, G. E. Scuseria and M. Ernzerhof, *J. Chem. Phys.*, 2003, **118**, 8207–8215.

31 J. Wróbel, K. J. Kurzydłowski, K. Hummer, G. Kresse and J. Piechota, *Phys. Rev. B: Condens. Matter Mater. Phys.*, 2009, **80**, 155124.

32 A. Alavi, P. Hu, T. Deutsch, P. L. Silvestrelli and J. Hutter, *Phys. Rev. Lett.*, 1998, **80**, 3650–3653.

33 H.-F. Wang, D. Wang, X. Liu, Y.-L. Guo, G.-Z. Lu and P. Hu, *ACS Catal.*, 2016, **6**, 5393–5398.

34 R. Kovacik, B. Meyer and D. Marx, *Angew. Chem., Int. Ed.*, 2007, **46**, 4894–4897.

35 N. R. D'Amico, G. Cantele and D. Ninno, *J. Phys. Chem. C*, 2012, **116**, 21391–21400.

36 M.-H. Liu, Y.-W. Chen, T.-S. Lin and C.-Y. Mou, *ACS Catal.*, 2018, **8**, 6862–6869.

37 D. Li, F. Xu, X. Tang, S. Dai, T. Pu, X. Liu, P. Tian, F. Xuan, Z. Xu, I. E. Wachs and M. Zhu, *Nat. Catal.*, 2022, **5**, 99–108.

38 J. H. Seinfeld and S. N. Pandis, *Atmospheric chemistry and physics: from air pollution to climate change*, John Wiley & Sons, Hoboken, New Jersey, 3rd edn, 2016.

39 Z.-Q. Wang, D.-R. Chu, H. Zhou and X.-P. Wu, *ACS Catal.*, 2022, **12**, 624–632.

40 H. Zhou, X.-P. Wu and X.-Q. Gong, *ChemCatChem*, 2022, **14**, e202101254.

41 Z. L. Wang, *Mater. Today*, 2004, **7**, 26–33.

42 J.-J. Liu, *Acta Phys. Sin.*, 2011, **60**, 037102.

43 Z.-Q. Wang, D. Wang and X.-Q. Gong, *ACS Catal.*, 2020, **10**, 586–594.

44 X.-P. Wu, X.-Q. Gong and G. Lu, *Phys. Chem. Chem. Phys.*, 2015, **17**, 3544–3549.

45 Z.-Q. Wang, H.-H. Liu, X.-P. Wu, P. Hu and X.-Q. Gong, *Catalysts*, 2022, **12**, 963.

46 S. Song, K. Yang, P. Zhang, Z. Wu, J. Li, H. Su, S. Dai, C. Xu, Z. Li, J. Liu and W. Song, *ACS Catal.*, 2022, **12**, 5997–6006.

47 H. Zhou, D. Wang and X.-Q. Gong, *J. Phys. Chem. C*, 2023, **127**, 11040–11045.

48 D. R. Aireddy and K. Ding, *ACS Catal.*, 2022, **12**, 4707–4723.

49 G. Griffin, *J. Catal.*, 1982, **73**, 396–405.

50 H. Chen, L. Lin, Y. Li, R. Wang, Z. Gong, Y. Cui, Y. Li, Y. Liu, X. Zhao, W. Huang, Q. Fu, F. Yang and X. Bao, *ACS Catal.*, 2019, **9**, 1373–1382.

51 D. Karhánek, dakarhanek/VASP-infrared-intensities (version v1.0) Zenodo, 2020.

52 S. Baroni, P. Giannozzi and A. Testa, *Phys. Rev. Lett.*, 1987, **58**, 1861–1864.

53 F. Boccuzzi, *J. Catal.*, 1978, **51**, 150–159.

54 R. P. Eischens, W. A. Pliskin and M. J. D. Low, *J. Catal.*, 1962, **1**, 180–191.

55 B. Yang, X.-M. Cao, X.-Q. Gong and P. Hu, *Phys. Chem. Chem. Phys.*, 2012, **14**, 3741–3745.

56 C. Copéret, D. P. Estes, K. Larmier and K. Searles, *Chem. Rev.*, 2016, **116**, 8463–8505.

57 Y. Wang, R. Kovacik, B. Meyer, K. Kotsis, D. Stodt, V. Staemmler, H. Qiu, F. Traeger, D. Langenberg, M. Muhler and C. Woll, *Angew. Chem., Int. Ed.*, 2007, **46**, 5624–5627.

58 W. Xiong, Z. Wu, X. Chen, J. Ding, A. Ye, W. Zhang and W. Huang, *Sci. China: Chem.*, 2024, **67**, 715–723.

59 X.-K. Wu, G.-J. Xia, Z. Huang, D. K. Rai, H. Zhao, J. Zhang, J. Yun and Y.-G. Wang, *Appl. Surf. Sci.*, 2020, **525**, 146481.

60 Q. Tang, Y. Lee, D.-Y. Li, W. Choi, C. W. Liu, D. Lee and D. Jiang, *J. Am. Chem. Soc.*, 2017, **139**, 9728–9736.

61 J. Wang, G. Li, Z. Li, C. Tang, Z. Feng, H. An, H. Liu, T. Liu and C. Li, *Sci. Adv.*, 2017, **3**, e1701290.

62 Z. Feng, C. Tang, P. Zhang, K. Li, G. Li, J. Wang, Z. Feng and C. Li, *J. Am. Chem. Soc.*, 2023, **145**, 12663–12672.